Editors' Suggestion   Featured in Physics

Blueprint for a Molecular-Spin Quantum Processor

A. Chiesa,[1,2,3] S. Roca,[4,5] S. Chicco,[1,3] M.C. de Ory,[6] A. Gómez-León,[7] A. Gomez,[6]
D. Zueco,[4,5] F. Luis,[4,5,*] and S. Carretta[1,2,3,†]

[1]*Università di Parma, Dipartimento di Scienze Matematiche, Fisiche e Informatiche, Parma I-43124, Italy*
[2]*INFN–Sezione di Milano-Bicocca, gruppo collegato di Parma, Parma 43124, Italy*
[3]*UdR Parma, INSTM, Parma I-43124, Italy*
[4]*Instituto de Nanociencia y Materiales de Aragón (INMA), CSIC-Universidad de Zaragoza, Zaragoza 50009,
Spain*
[5]*Departamento de Física de la Materia Condensada, Universidad de Zaragoza, Zaragoza 50009, Spain*
[6]*Centro de Astrobiología (CSIC - INTA), Torrejón de Ardoz, Madrid 28850, Spain*
[7]*Instituto de Física Fundamental, IFF-CSIC, Madrid 28006, Spain*

The implementation of a universal quantum processor still poses fundamental issues related to error mitigation and correction, which demand investigation of also platforms and computing schemes alternative to the main stream. A possibility is offered by employing multilevel logical units (qudits), naturally provided by molecular spins. Here we present the blueprint of a molecular spin quantum processor consisting of single molecular nanomagnets, acting as qudits, placed within superconducting resonators adapted to the size and interactions of these molecules to achieve a strong single spin-to-photon coupling. We show how to implement a universal set of gates in such a platform and to readout the final qudit state. Single-qudit unitaries (potentially embedding multiple qubits) are implemented by fast classical drives, while an alternative scheme is introduced to obtain two-qubit gates via resonant photon exchange. The latter is compared to the dispersive approach, finding in general a significant improvement. The performance of the platform is assessed by realistic numerical simulations of gate sequences, such as Deutsch-Josza and quantum simulation algorithms. The very good results demonstrate the feasibility of the molecular route towards a universal quantum processor.

I. INTRODUCTION

Recent advances in the realization of quantum chips with gradually better performances (both in the number of qubits and in the fidelity of operations) [1–8] could stimulate the question: is it still worth to pursue other routes different from the most established technologies? Are there fundamental issues (not barely technical problems), which could be more easily tackled by alternative platforms, potentially in the short term?

One should first acknowledge that even the most advanced platforms, i.e., superconducting qubits and ion traps, are still limited by key errors in the manipulation of a relevant number of qubits, thus placing the actual implementation of a universal, error-corrected hardware still far from current capabilities. A promising option to strongly mitigate errors and simplify quantum operations is to move from the binary qubit logic to the use of multilevel logical units called *qudits*. In fact, qudits can be exploited to reduce the number of required entangling gates in the synthesis of arbitrary unitaries [9], with potentially disruptive applications in quantum simulation [10] and quantum error correction [11–13].

In this respect, it was shown that molecular spin systems such as molecular nanomagnets (MNMs) could constitute the natural playground [14]. Indeed, they can provide many low-energy states with naturally long coherence [15–18], which can be engineered by chemistry to achieve an impressive degree of control, thus meeting the requirements of tailored quantum computing [19–21], quantum simulation [22,23], and quantum error-correction [12,24,25] schemes. The fundamental limitation toward the realization of a MNM-based quantum hardware is represented by the realization of a scalable platform in which individual molecules are initialized, manipulated, and readout. The natural way of achieving this is to export standard methods from superconducting qubits' technology [26–29], i.e., to couple MNMs to on-chip

---

*fluis@unizar.es
†stefano.carretta@unipr.it

superconducting resonators and exploit the tools of circuit quantum electro-dynamics to "wire them up." This idea was already put forward in Ref. [30], but it has remained a long-term vision until recent progresses both in increasing the coupling of spins to superconducting resonators [31–34] and in understanding the crucial advantage of molecular qudits for quantum information processing [14]. Indeed, on the one hand, the fabrication of nanoscopic constrictions on the transmission lines allow one to concentrate the magnetic field in regions where MNMs of the same size can be naturally accommodated. This enhances the spin-photon coupling by orders of magnitude, as experimentally demonstrated [31,32]. On the other hand, the potentiality of properly designed molecular spins to encode qudits with suppressed decoherence [35,36] or embedded quantum error correction [13,35,37–39] has been investigated. Hence, we are now in a position to understand and quantify advantages and limitations of a quantum hardware consisting of individual MNMs coupled to superconducting resonators. This requires a scheme for implementing qudit gates and for reading the output, a suitable design of the platform and accurate simulations to figure out where we are and what we can eventually accomplish.

To this end, we present hereafter the blueprint of a molecular spin quantum processor (MSQP). Both superconducting resonators and MNM qudits embedded within them are designed to achieve a strong coupling to single photons, by locally concentrating the microwave magnetic field and choosing suitable molecular states.

We illustrate how to implement a universal set of gates in such a platform and how to readout the final qudit state. In particular, we show that several qubits can be encoded within an individual qudit and single-qudit unitaries corresponding to multiqubit algorithms can be implemented by classical drives sent through proper auxiliary control lines [30]. Moreover, we propose an alternative scheme to obtain two-qudit gates by means of a relatively fast resonant real photon exchange [40,41], using the tunability of the resonator frequency as the unique knob [42]. This scheme is compared with a dispersive approach [43] for the implementation of two-qudit gates by virtual photon exchange, finding a useful speedup for the former and hence an improved fidelity, due to the limited effect of decoherence. The overall performance of the proposal is assessed through realistic simulations of elementary gates and of more complex sequences, such as those involved in the Deutsch-Josza algorithm implemented on a single qudit and in the quantum simulation of interesting physical models. Our simulations take into account the most paramount errors occurring on a real platform, namely photon loss and pure dephasing of individual spins. The very promising results achieved with experimentally reachable conditions demonstrate that a MSQP could be a valid path toward a universal quantum hardware.

The paper is organized as follows: we first present the working principles of the MSQP (Sec. II) and then move to the design of the resonator, along with the estimate of feasible spin-photon coupling strengths (Sec. III). Then we simulate the related performance of the hardware (Sec. IV) for elementary gates and for more complex quantum simulation sequences. We finally summarize results and discuss perspectives for further steps in Sec. V.

II. WORKING PRINCIPLES OF THE MOLECULAR SPIN QUANTUM PROCESSOR

We illustrate below the working principles of our MSQP. In particular, we first introduce the static system Hamiltonian and basic ideas to choose the optimal spin system. Then, we show how each of the five DiVincenzo criteria can be fulfilled.

For sake of clarity, we start here by considering an elementary unit of the MSQP, consisting of a single resonator embedding two molecular spin qudits, both strongly coupled to the photon field. The scheme can then be easily generalized to an array of such units, as explained below (Sec. II F). Each unit of the scalable architecture is described by the following Hamiltonian:

$$H = H_p + H_S + H_{Sp}. \tag{1}$$

Here the first term $H_p = \hbar\omega_r(t)\left(a^\dagger a + 1/2\right)$ represents the photon field of tunable frequency $\omega_r(t) = \omega_0 + \delta(t)$ around a central value ω_0, with $a^\dagger$ (a) boson creation (annihilation) operators satisfying $[a, a^\dagger] = 1$.

The second term in Eq. (1) is the spin Hamiltonian of two spin S qudits:

$$H_S = \mu_B B \sum_{i=1,2} g_i S_{zi} + \sum_{i=1,2} D_i S_{zi}^2, \tag{2}$$

consisting of the Zeeman interaction with an external field and of a zero-field splitting anisotropy term, which is essential to make all the energy gaps inequivalent and hence individually addressable by resonant pulses. The eigenstates of H_S are the same as S_z ($|m_i\rangle$), with energies $E_{m_i} = D_i m_i^2 + g_i \mu_B B m_i$ and allowed $|m_i\rangle \rightarrow |m_i \pm 1\rangle$ dipole transitions. (We omit here for simplicity other possible anisotropic terms, which do not qualitatively alter our results.)

Finally, H_{Sp} represents the spin-photon interaction contribution, given by

$$H_{Sp} = \sum_{i=1,2} 2G_i(a + a^\dagger)S_{xi}$$

$$\approx \sum_{i,m} G_i^m(a|m+1\rangle\langle m| + a^\dagger|m\rangle\langle m+1|), \tag{3}$$

where in the second line $G_i^m = G_i\sqrt{S(S+1) - m(m+1)}$ and we apply the rotating-wave approximation (RWA),

which is practically exact in the examined range of parameters. Even though not employed in our numerical simulations, the RWA allows us to perform all of the following reasoning with only energy-conserving terms. From Eq. (3) we note that the coupling of the resonator field with each spin transition G_i^m (and hence the time required to implement two-qudit gates) can be enhanced by proper choice of the spin system and of the transitions, besides resonator engineering. Such a degree of freedom is a rather unique opportunity offered by molecular nanomagnets, which can be exploited to significant speedup two-qudit gates. In particular, for a spin S system described by Hamiltonian (2), transitions between $|m_i = 0\rangle$ and $|m_i = \pm 1\rangle$ states (the lowest energy ones in the presence of easy plane anisotropy and at low field) are enhanced by a factor $\sqrt{S(S+1)}$ compared to a spin 1/2. To fully exploit this degree of freedom, we consider in the following two $S = 10$ qudits, with $D_i/2\pi \approx 7 - 8$ GHz and spin transitions always involving a $|m_i = 0\rangle$ state (here and in the following, parameters are in units of $\hbar$). Although not corresponding to a specific molecule, the assumed parameters are perfectly reasonable. Indeed, the employed $|D|$ are exactly in between those of the two most famous $S = 10$ single-molecule magnets, namely Fe_8 [44] and Mn_{12} [45,46]. Moreover, multispin clusters with easy plane anisotropy ($D_i > 0$) have also been already synthesized (see, e.g., an $S = 6$ Cr_{12} [47] with $D/2\pi = 2.6$ GHz), and examples exist even with much larger S [48], although with smaller or less characterized anisotropy.

In the following subsections we address one by one the DiVincenzo criteria.

A. Encoding and initialization

In the idle configuration [i.e., with $\delta(t) = 0$], the couplings G_i^m are much smaller than the difference between the bare photon ($\hbar\omega_0$) and spin [$E_{mm'}^{q_i} = E_m^{(q_i)} - E_{m'}^{(q_i)}$] excitation energies, for each qudit q_i. Hence, the eigenstates of Hamiltonian (1) are practically factorized and can be expressed as $|m_1 m_2\rangle \otimes |n_p\rangle$, with $S_{zi}|m_i\rangle = m_i|m_i\rangle$ and $a^\dagger a|n_p\rangle = n_p|n_p\rangle$.

Then, we encode two-qudit logical states in the zero-photon subspace $\langle a^\dagger a \rangle = 0$, i.e., we represent the two-qudit wave function as $|pq\rangle \equiv |m_1 m_2\rangle \otimes |n_p = 0\rangle$. This choice reduces the harmful effect of photon loss. Hereafter, we relabel the states with $p, q = 0, \ldots, 2S$ in order of increasing energy. With the parameters considered in the text (i.e., low B and $D_i > 0$), the sequence of single-qudit states is given by $m_i = 0, -1, +1, -2, +2, \ldots$, as shown in Fig. 1.

By working at a base temperature below 10 mK (corresponding to a frequency of approximately equal to 0.2 GHz), high-fidelity initialization of each qudit in its ground state can be achieved by cooling.
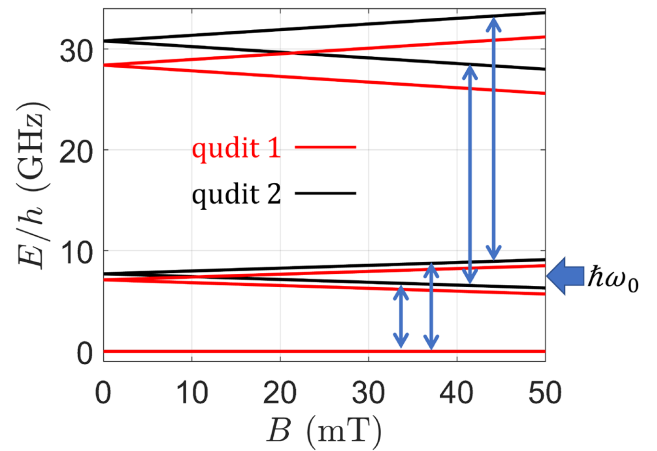

FIG. 1. Lowest energy levels for the two qudits used in the reported simulations, with $D_1/2\pi = 7.1$ GHz, $D_2/2\pi = 7.7$ GHz, $g_i = 2$. Blue double arrows indicate allowed EPR transitions for qudit 2 between $|m_2\rangle \to |m_2 \pm 1\rangle$ levels, induced by resonant (low-power) microwave classical pulses in the range 5–20 GHz. An analogous situation is found for qudit 1 (not shown for clarity). The thick arrow on the right indicates the bare resonator frequency $\hbar\omega_0$.

B. Single-qudit gates

In analogy to what is usually done for qubits, a universal qudit set can be obtained by combining general single-qudit gates with one two-qudit entangling gate [36,49].

As far as the former are concerned, any single-qudit unitary can be decomposed into approximately d^2 Givens rotations [49] between consecutive $|m\rangle \to |m \pm 1\rangle$ transitions.

These transitions are indicated by blue arrows in Fig. 1 and can be accomplished by classical control drives $H_1(t) = B_1 \theta(|t - t_0| - \tau)\mu_B \cos(\omega t + \phi)(g_1 S_{y1} + g_2 S_{y2})$ resonant with the addressed pair of levels. With the here employed parameters, this sets the driving frequency in the 5–20 GHz range, perfectly achievable using low-power pulses, i.e., $B_1 \sim 1$–5 G. Using larger values of B_1 (faster pulses) would only increase leakage towards other transitions (different from the addressed one) without significantly reducing the time to implement a generic algorithm. Indeed, even with small B_1, the latter is largely dominated by the duration of two-qudit gates, as discussed below. In the near future, the performance of single-qudit gates (both in terms of gating time and leakage reduction) could be further improved by optimal quantum control techniques [50].

In the current development stage, noise is particularly relevant for multiqubit gates, while manipulations on individual objects (i.e., a single qubit-qudit) are much easier. Hence, an interesting perspective in the near term is to embed several qubits into a single qudit and then rewrite multiqubit algorithms in terms of single-qudit transitions

and gates. This requires proper development of a dictionary to map multiqubit into single-qudit operations. Such a dictionary must include the correspondence between the eigenstates of the multiqubit and of the qudit system. This allocation of levels can be chosen arbitrarily depending on the connectivity between levels in our qudit. For example, we can assign the multiqubit levels on which most operations are to be acted upon to the levels which can be manipulated faster. Once such a structure is constructed, we decompose the unitary that comprises the whole multiqubit circuit into single-qudit operations (or Givens rotations) using a QR decomposition method [36,49,50]. With this method, we can decompose any unitary matrix U into the product $U = QR$, where Q is an orthogonal matrix that will be the sequence of different pulses and R is a diagonal matrix that will account for the relative phases induced by the operations between the qudit levels. More explicitly, the operations that we apply to our molecule have the following Givens rotation representation $R_{m,m+1}(\theta, \varphi) = g_{m,m+1}(\theta, \varphi) \oplus I_{\overline{(m,m+1)}}$, where

$$g_{m,m+1}(\theta, \varphi) = \begin{bmatrix} c & s \\ -s^* & c \end{bmatrix},$$

with $c = \cos(\theta/2)$ and $s = -i\sin(\theta/2)e^{i\varphi}$, is the two-level rotation on the levels m, $m + 1$ and $I_{\overline{(m,m+1)}}$ is the identity over the rest of qudit levels. By choosing properly θ and ϕ we can transform our unitary U into the diagonal matrix R: $R = \left(\prod_i \prod_m R_{m,m+1}(\theta^i, \varphi^i)\right)^\dagger U$. This diagonal matrix can be further transformed into the identity applying two-level rotations around the Z axis, which can be achieved from the previous ones: $R^Z_{m,m+1}(\theta) = R_{m,m+1}(\pi/2, \pi)R_{m,m+1}(\theta, \pi/2)R_{m,m+1}(\pi/2, 0)$ (cf. Appendix A in Ref. [50] for a detailed description of the algorithm). With these definitions we have everything that is needed to decompose any multiqubit circuit into a single-qudit one. We now need to find the relation between the decomposition parameters (θ, φ) and the physical ones that we are able to implement.

In order to get the physical parameters that are needed for implementing such decomposition, we rewrite $H_1(t)$ within the RWA and in interaction picture, setting for each $|m\rangle \to |m'\rangle$ transition $\hbar\omega = E^{q_i}_{mm'}$. Then we get

$$H^{\text{int}}_1 \approx \frac{1}{2} g\mu_B B_1 |\langle m| S_y |m'\rangle| \left(e^{-i\varphi} |m\rangle \langle m'| + \text{h.c.}\right). \quad (4)$$

Here, the angle $\varphi = \phi - \delta$ results from the phase of the driving pulse, ϕ, and from the possible phase induced in the transition between levels (here $\delta = \pi/2$, since we choose an oscillating field along y). From here, the unitary evolution of the system in the interaction picture reads

$$U^{\text{int}}(t) = \exp\left[-i\frac{\theta(t)}{2}\left(\cos\varphi \sigma^{mm'}_x - \sin\varphi \sigma^{mm'}_y\right)\right], \quad (5)$$

with $\theta(t) = g\mu_B B_1 |\langle m| S_y |m'\rangle| t$ and where the $\sigma^{mm'}_\alpha$ ($\alpha = x, y$) operators act as the Pauli operators in the subspace of the two levels involved in the transition $|m\rangle \to |m'\rangle$. $U^{\text{int}}(t)$ is precisely the kind of rotations we get from our decomposition algorithm: θ modulates the population transfer between levels and φ the relative phase acquired. Therefore, we can construct directly the experimental pulses that are needed to implement any multiqubit circuit in our molecule from the sequence of operations that we obtain from the QR decomposition.

C. Two-qudit gates

Terrific advances have been recently done in increasing single spin to photon couplings [31,32] and estimates for $G_i/2\pi$ can reach values in the order of 10^2 kHz for a spin 1/2, as demonstrated in Sec. III below. Nevertheless, these numbers still require a careful engineering of photon-mediated two-qudit gates in order to keep gating times (τ_{2q}) significantly shorter than the system coherence. Indeed, the established scheme to implement two-qubit gates in the dispersive regime [51] implies rather long τ_{2q}, thus making its realization practically difficult. Even for qudits, where additional strategies to optimize the coupling and reduce the required interaction time can be considered [43]. To overcome this limitation, we introduce below an alternative scheme, which significantly shortens τ_{2q} by operating in the resonant regime.

Before illustrating our proposal, we recall the working principles of the dispersive approach. The idea is analogous to the first proposals on transmon qubits [26]. If we consider a pair of spins coupled to the same resonator and such that the spin gaps ($E^{q_i}_{mm'}$) are significantly detuned from $\hbar\omega_r$ (i.e., $G^m_i \ll |\hbar\omega_r - E^{q_i}_{mm'}|$), we can derive a second-order effective spin-spin interaction mediated by the virtual exchange of a photon [14], of the form

$$H_{\text{eff}} = \sum_{m,m'} \Gamma^{m',m'\mp 1}_{m,m\pm 1} |m, m'\rangle \langle m \pm 1, m' \mp 1|, \quad (6)$$

with $\Gamma^{m',m'\mp 1}_{m,m\pm 1} \approx G^m_1 G^{m'}_2 / \Delta_i$ and $\Delta_i = \hbar\omega_r - E^{q_i}_{m,m\pm 1}$. Now, if the two spin gaps are significantly different $|E^{q_1}_{m,m\pm 1} - E^{q_2}_{m',m'\mp 1}| \gg \Gamma^{m',m'\mp 1}_{m,m\pm 1}$, H_{eff} is ineffective and the two qudits are decoupled. This occurs, for instance, if the two molecules have slightly different g_i or D_i in Eq. (2). To turn on the mutual spin-spin interaction, we can apply local magnetic fields [30] to make $E^{q_1}_{m,m\pm 1} = E^{q_2}_{m',m'\mp 1}$, thus activating an oscillation between $|m, m'\rangle$ and $|m \pm 1, m' \mp 1\rangle$ two-qudit states.

In the case of qubits, the resulting evolution $U_{XY}(\tau)$ is equivalent to that induced by a spin Hamiltonian of the form $H_{XY} = s_{x1}s_{x2} + s_{y1}s_{y2}$, i.e., $U_{XY}(\tau) = \exp[-iH_{XY}\tau/\hbar]$. Hence, the unitary gate $U_{XY}(\tau)$ can be naturally exploited in the quantum simulation of several

models, which can be mapped to this Hamiltonian, as illustrated below. For proper choice of the interaction time τ, this evolution implements entangling gates such as the *i*SWAP or the $\sqrt{i\text{SWAP}}$. The resulting gating time (to implement, e.g., an *i*SWAP) is given by $\tau_{2q} = \pi\Delta/2(G_i^m)^2$. With the parameters employed here, $\tau_{2q} \sim 6$ μs, thus making two-qudit gates implemented with the dispersive approach rather slow and hence prone to decoherence.

We now move to our alternative proposal for two-qudit gates in the resonant regime, i.e., by real (rather than virtual) photon exchange. This leads to gate times scaling linearly (instead of quadratically) with G_i^m, achieving a significant speedup compared to the dispersive regime. In particular, we consider a *qudit controlled-phase gate*, in which a desired phase φ is added only to a specific component $|\bar{p}\bar{q}\rangle$ of the two-qudit wave function. This corresponds to the unitary transformation

$$U_\varphi^{\bar{p}\bar{q}} = e^{-i\varphi} |\bar{p}\bar{q}\rangle \langle\bar{p}\bar{q}|$$
$$+ \sum_{p,q} |pq\rangle \langle pq| (1 - \delta_{pq,\bar{p}\bar{q}}). \quad (7)$$

To minimize the duration of the two-qudit gate, we exploit only transitions among the lowest m states (i.e., $|m = 0\rangle \leftrightarrow |m = \pm 1\rangle$) in the level diagram of Fig. 1, thus getting an enhancement of the coupling of $\sqrt{S(S+1)} \approx 10$. In the example below, this allows us to directly implement U_φ^{01}, which can be easily transformed into any other U_φ^{pq} gate by adding single-qudit gates implemented via much faster classical resonant pulses. This not only guarantees qudit universality, but also a relevant flexibility in the two-qudit gate, which could be very useful to reduce the depth of many algorithms.

To illustrate the implementation of a generic U_φ^{pq} gate, we refer to the scheme reported in Fig. 2. In particular, we consider a three-level qudit q_1 (including an auxiliary level $|e\rangle$ exploited during the gate) and a four-level qudit q_2, but the scheme can be straightforwardly extended to qudits of different size. As a unique knob to implement the gate, we exploit the tunability of the resonator frequency by insertion of proper superconducting quantum interference device (SQUID) elements. Such a tunability can reach about 30 % of the bare frequency ω_0 with a reduction of the resonator quality factor Q of only a factor of 2–3 [42] and can be as fast as 1 ns [52].

We then proceed along the following steps (see Fig. 2):

(a) In the idle phase the resonator frequency is set off resonance from all qudit excitations [Fig. 2(a)] and no photons are present (dark resonator).

(b) We then bring the resonator into resonance with $E_{01}^{(q_2)}$, i.e., the $|0\rangle \leftrightarrow |1\rangle$ transition of q_2 [Fig. 2(b)]. If state
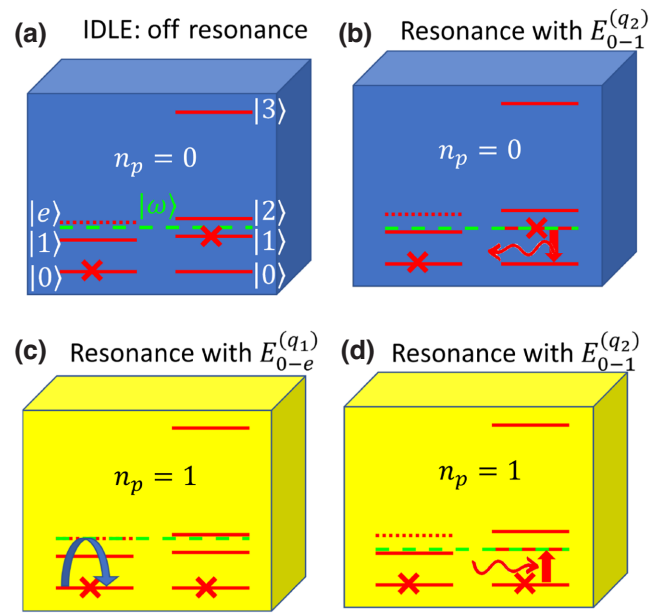

FIG. 2. Scheme of the two-qudit resonant gate: dark (bright) boxes indicate empty (single photon) resonators. Two photon states (included in the simulations) are never populated. Energy levels of the two qudits are indicated by red lines. In this example, we use two levels to encode the logical state of q_1 (left) and four to encode q_2 (right), while the second excited state of q_1 (dotted line, $|e\rangle$) is an auxiliary one exploited during the gate. The dashed green line indicates the resonator frequency, which is varied at each step. We illustrate the steps of the gate for a system prepared in $|01\rangle$ (crosses). (a) Idle state, with no photons (dark) and the resonator out of resonance with respect to all qudit transitions. (b) The resonator is brought into resonance with $E_{01}^{(q_2)}$ and a photon is emitted if q_2 is prepared in $|1\rangle$. (c) A photon is now in the resonator (bright) and can be absorbed emitted if q_1 is prepared in $|0\rangle$, once the resonator is brought into resonance with $E_{0e}^{(q_1)}$. (d) The resonator is brought again into resonance with $E_{01}^{(q_2)}$ and the photon is absorbed, ending up again with $|01\rangle$ and an additional phase.

$|1\rangle$ of q_2 is populated, a photon is emitted and the resonator becomes bright (c).

(c) We then induce a 2π transition from $|0\rangle$ to $|e\rangle$ on q_1 [Fig. 2(c)] with photon absorption and re-emission. If the transition is *resonant*, the amplitude is completely transferred from $|0\rangle$ to $|e\rangle$ and back, resulting in a π phase added to the $|01\rangle$ component of the two-qudit wave function. If we slightly detune the excitation from resonance (the so-called *semiresonance*), only part of the amplitude is temporarily excited to $|e\rangle$ and comes back with an additional phase, which can be chosen by setting the detuning [41]. In this way, we add an arbitrary phase to $|01\rangle$.

(d) Finally [Fig. 2(d)], we bring again the resonator into resonance with $E_{01}^{(q_2)}$. For the initial component $|1\rangle$ on q_2 [which emits the photon in (b)] the photon is absorbed again and we go back to $|01\rangle$ with no photons in the

resonator and the additional phase inherited from the previous step. The time interval between steps (b) and (d) can be adjusted in order to compensate any additional phase acquired, so that only (c) introduces a two-qudit phase. This happens only for the $|01\rangle$ component, while all the others are left unaffected by the sequence. Hence, the whole sequence implements U_φ^{01}, as desired.

We conclude this section by noting that, although significantly slower, the dispersive approach has some significant advantages, which must be kept in mind. In particular, gates are practically insensitive to photon loss, which instead becomes more relevant in the resonant regime. Hence, a quantitative comparison between the two methods is needed, as reported in Sec. IV below.

D. Readout

We provide here two different strategies to readout the final state of a qudit strongly coupled to a superconducting resonator. Analogously to two-qudit gates, these two strategies are designed to work either (i) in the dispersive or (ii) in the resonant regimes.

Case (i) (proposed in Ref. [53]) mimics the approach followed with superconducting qubits and relies on transmission measurements in the dispersive regime. The resonator frequency experiences a shift χ that depends on the qudit state and that is proportional to the dispersive resonator-qudit coupling. More specifically, it scales as $(G_i^m)^2/\Delta$. Well-known advantages of this readout technique are its single-shot nature and that it is a quantum nondemolition measurement [51].

The alternative approach (ii) we propose here is based again on resonant photon emission, as illustrated in Fig. 3. In practice, it is equivalent to swap the quantum state we want to detect from the qudit to the resonator (by bringing a specific qudit gap into resonance with the photon field for a time $\pi/2G$), detect the possible presence of a photon in the resonator and swap the projected state back by a classical drive depending on the measurement outcome. This effectively implements a projective measurement on the qubit. Extension to the qudit case is straightforward, by addressing different spin gaps one at a time.

The readout fidelity of (i) depends on a proper discrimination of the resonator shift χ. Hence, the main limitation comes from the broadening of the resonance peaks, mainly due to resonator losses and to spin dephasing of the qudit, as discussed in the next subsection (Sec. II E). This broadening must be smaller than the frequency separation associated with each qudit state. The effect can be partially mitigated by measuring the transmission phase rather than its modulus, as it seems to be more insensitive to broadening [53].

In addition, the time needed to complete the readout process scales as $1/\chi$. Readout times of the order
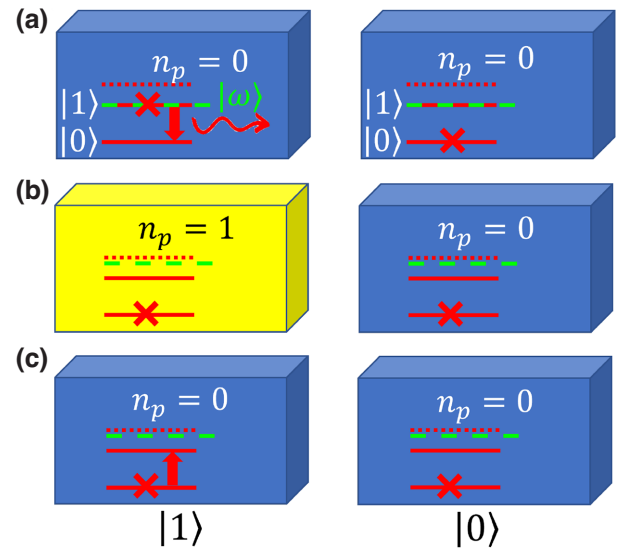

FIG. 3. Scheme of the resonant readout of a qubit in state $|0\rangle$ (left) or $|1\rangle$ (right). (a) Starting with no photons (dark cavity) the resonator is brought into resonance with E_{01}. If the qubit is in state $|1\rangle$ (left) a photon is emitted and the cavity becomes bright (b), bringing the qubit to the ground state. At this step, a single-photon counter detects the possible presence of the photon (and annihilates it). In the case of positive outcome, a classical drive sends back the qubit state to $|1\rangle$ (c), thus implementing a projective measurement on the qubit.

of 50–100 ns have been achieved with superconducting transmons having $\chi = 7.9$ MHz and operating at $G/\Delta \sim 1/10$, using high-sensitivity detection stages, involving parametric amplification [54]. Applying similar detection conditions, we expect χ to be approximately 2 orders of magnitude smaller in our MSQP, with corresponding readout times of approximately 5–10 μs. For algorithms that do not involve any measurement-dependent feedback during the execution process, the readout time needs to be sufficiently short as compared to the spin relaxation time T_1. This requirement does not pose a very stringent limitation, as T_1 becomes rather long at very low temperatures. Yet, if one attempts to implement quantum error-correction codes, then the limiting time scale is the spin coherence time T_2, thus it might be necessary to look for faster methods.

The resonant approach (ii) provides such a large speedup. It will also increase the readout fidelity, by reducing the harmful effects of both spin decoherence and resonator losses. Indeed, the time required to implement a resonant readout is dominated by the time for photon emission (approximately equal to 250 ns for the lowest energy gap of the $S = 10$ molecule considered here), while single-photon detectors can work as fast as 50–100 ns [55].

In summary, resonant and dispersive readout provide different ways to measure the state of the qudits. Each regime of operation comes with certain advantages and

disadvantages, which is why different experimental setups might embrace different options. The dispersive regime is nondemolition, but it is much slower due to the small dispersive spin-resonator coupling. In addition, it requires the design of more complex protocols, especially in the case of qudits with a large number of levels [53]. In terms of decoherence, it is mainly limited by spin dephasing. In contrast, the resonant readout is a projective measurement that can be applied to any given pair of levels. In this regime, the effect of photon loss is expected to increase, but the significant speedup which is achieved makes it practically negligible.

In both cases, the most direct way to improve the readout fidelity is to increase the spin-photon coupling G_i^m, such that in scheme (i) transmission peaks are more separated and the readout time is shorter, whereas in scheme (ii) resonant photon emission becomes faster.

E. Decoherence

The most important decoherence channels in our platform are represented by (i) photon loss and single-molecule (ii) pure dephasing, originating at low temperature from the interaction between the central spin and the surrounding nuclear spin bath [38].

As already noted above, photon loss (occurring at a rate $\omega_r/2\pi Q$, with Q the resonator quality factor) is a much more crucial effect in the resonant compared to the dispersive regime, due to real (rather than virtual) photon exchange. Nevertheless, by encoding the logical state within the $n_p = 0$ subspace, this effect is largely reduced and limited to the resonant emission and absorption processes of two-qudit gates and readout. In all other steps of computation (namely single qudit rotations and idle phases) photon loss is irrelevant.

As far as spin dephasing is concerned, a high-fidelity two-qudit gate requires coherence time T_2 significantly longer than the gating time τ_{2q}. With the present parameters $\tau_{2q} \sim \mu s$ in the resonant regime, thus requiring $T_2 > 50$ μs to achieve high-fidelity gates. Remarkably, these values have already been experimentally accomplished by proper chemical optimization of the molecular structure, combined with deuteration and dilution, in V/Cu complexes [17,56], reaching even the ms range [15]. Moreover, it is worthwhile to note that the setup we are considering here will work (i) at much lower temperatures than those usually employed in T_2 measurements and (ii) at the single-molecule level, where a possible distribution of anisotropy orientations observed in a crystal will no longer be an issue. Hence, by working on properly engineered single molecules and in the mK region, coherence times approaching ms can be expected.

F. Scalability

Having introduced all the working principles of the elementary unit of the MSQP, we can now address the final scalability issue.

One of the appealing features of this approach is that the MSQP can be scaled up at different levels. First, by chemical design that brings in multiple states within each molecular unit. Eventually, this would allow proof-of-concept implementations of qudit-based algorithms even working with molecular crystals. Yet, moving beyond the Hilbert space provided by each molecule relies on the coupling to a superconducting circuit. Several molecular spin qudits can be integrated within a superconducting resonator, up to the limit allowed by nanofabrication techniques (as molecules themselves are microscopic entities). Finally, one can consider an array of capacitively coupled resonators, each one containing a single or a few molecular qudits strongly coupled to the local photon mode, described by the boson field $\hbar\omega_{r,i}(a_i^\dagger a_i + 1/2)$. The capacitive coupling between neighboring resonators is described (in the rotating-wave approximation) by an interaction term of the form $\kappa a_i^\dagger a_j + \text{h.c.}$, with $\kappa/2\pi$ in the 10–25 MHz range [57]. Neighboring resonators are characterized by different bare frequencies (i.e., $|\omega_{0i} - \omega_{0j}| >> \kappa$), so that the intercavity photon hopping is effectively turned off in the idle phase.

To implement two-qudit gates between molecules placed into different resonators, we proceed in a way analogous to that illustrated in Fig. 2, but with an additional step. The two qudits we consider can now be located into neighboring resonators i and j. Hence, after photon emission in step (b), one needs to bring resonators i and j into mutual resonance, i.e., make $\omega_{0i} = \omega_{0j}$, thus inducing hopping of the single photon from the resonator containing qudit 2 to that containing qudit 1. We then proceed with photon absorption and re-emission as in Fig. 2(c) and repeat the previous steps of photon hopping and reabsorption, as in Fig. 2(d), eventually implementing the same U_φ^{pq} gate illustrated above.

III. SYSTEM LAYOUT AND TECHNICAL ASPECTS

We now present in more detail the layout of the MSQP elementary unit, together with numerical estimates of the spin-photon coupling, which can be accomplished by a proper design.

The basic unit of our platform is schematically shown in Fig. 4. It consists of two molecular spin qudits coupled to a resonator, whose resonant frequency ω_r can be tuned by means of a SQUID. As explained above, the resonator reads out the spin states and mediates an effective interaction between the two qudits that allows performing conditional quantum operations. The circuit includes also
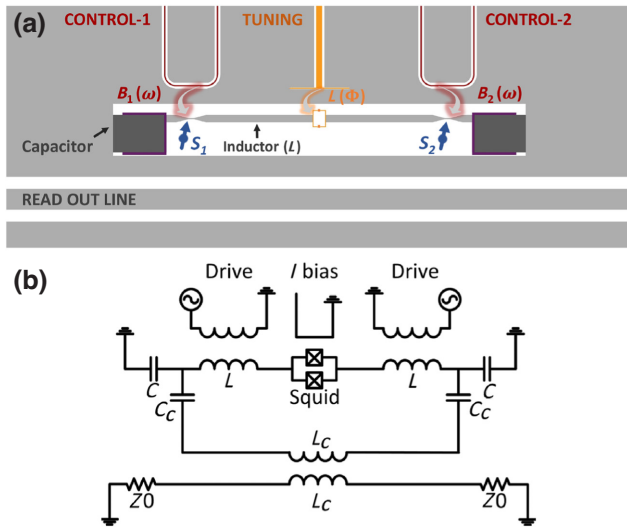
FIG. 4. Schematic layout (a) and electric circuit (b) of the MSQP elementary unit, which consists of an on-chip *LC* superconducting resonator with a few magnetic molecules deposited on top. Nanosized constrictions concentrate the magnetic field at specific regions, where the coupling to single molecules, with spins $\mathbf{S}_1$ and $\mathbf{S}_2$ is enhanced. Transmission lines introduce electromagnetic pulses to coherently control each spin qudit and to tune the flux though a dc SQUID in series with the inductor. The latter serves to tune the resonator characteristic frequency. An additional transmission line reads out the state of the resonator, which provides information on the spin-qudit states.

FIG. 5. (a) Layout of a 7.5-GHz *LC* superconducting resonator with a 22-μm-long and 4-μm-wide inductor and two parallel plate capacitors. (b) Two-dimensional plot of the distribution of currents at resonance. (c) Spatial dependence of the microwave magnetic field generated by the resonator for different inductor widths *w*.

control transmission lines, which generate local magnetic field pulses to control the spin states of each qudit and the flux through the SQUID loop, and a readout line. Since the aim of this work is to discuss its operation and potential based on a realistic layout, we provide here estimations for all relevant parameters based on circuits that are feasible.

As the previous sections show, the main technical challenge behind this proposal is the achievement of a spin-photon coupling that is sufficiently strong as compared to the decoherence rates of the spins (typically determined by $1/T_2$) and the photons ($\omega_r/2\pi Q$). Values of Q in the range $5 \times 10^5 - 10^6$, corresponding to photon line widths of the order of 1–10 kHz, can be achieved for 3–8 GHz resonators [58].

For this reason, we consider here a circuit designed to maximize and then also confine the superconducting current in resonance, thus enhancing the photon magnetic field in a nanoscopic region. The circuit consists of a lumped-element *LC* resonator, made of two capacitors connected by a single-wire inductor [Fig. 5(a)]. These resonators provide ample room for tuning relevant parameters, such as impedance *L* and resonance frequency, without compromising the transmission through the readout line that carries information about the system state. Moreover, several of them can be coupled to a single transmission line. Parallel plate capacitors are employed as they are free
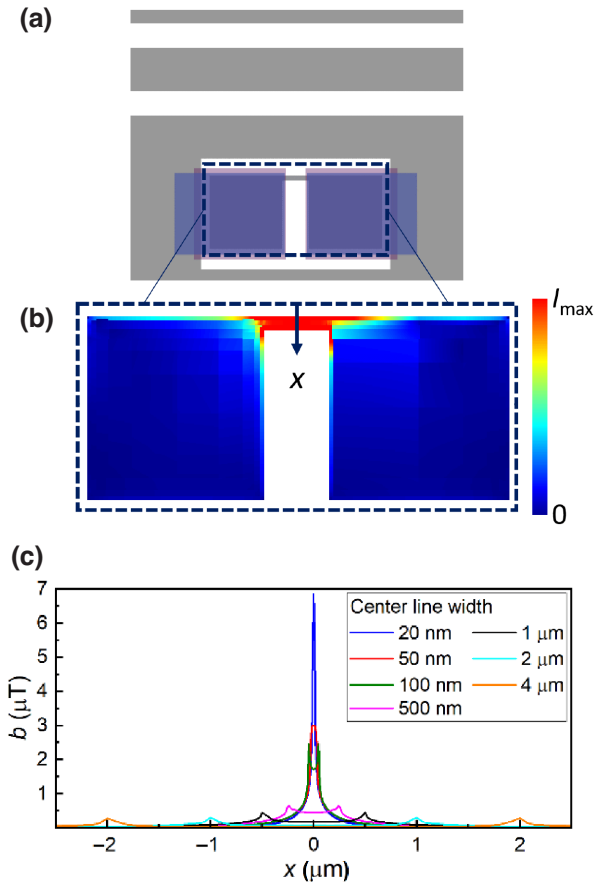
from parasitic inductances present in other designs, such as interdigitated capacitors. This reduces the mode volume, confining the current *I* almost completely in the inductor, as shown in Fig. 5(b). Near resonance, the photon energy splits equally between the magnetic and electric components. Since the former equals $LI^2/2$, a very low inductance leads to large current intensities for single-photon excitations. The circuit shown in Fig. 5 has a 22-μm-long, 4-μm-wide, and 100-nm-thick Nb inductor. We simulate its electromagnetic response using the SONNET package [59]. This gives a resonator inductance $L \simeq 12.9$ pH, leading to a rms current $I_{\mathrm{rms}} = \sqrt{\hbar\omega_r/2L} \simeq 438$ nA. In the simulation we consider a kinetic inductance of 0.1 pH/sq, corresponding to a 100-nm Nb film.

The photon magnetic field **b**, which determines the coupling to the spins, is then calculated with the 3D-MLSI simulation package [60]. The input parameters are the rms current (438 nA) flowing through the inductor and the London penetration depth of Nb $\lambda_L \simeq 90$ nm. An example of

the magnetic field intensity obtained at a distance of 1 nm above the chip's surface is shown in Fig. 5(c). For the original inductor width $w = 4$ μm, it peaks at values below 0.4 μT near the inductor edges.

A way to further enhance b at specific locations is to locally confine the current by fabricating nanoconstrictions in the inductor line [61]. Such constrictions can be made by ion-beam lithography and they do not significantly affect the resonator's properties provided that they are sufficiently short (below 1 μm) [61]. Figure 5 shows how b increases as the constriction width w is decreased, reaching values close to 7 μT for $w = 20$ nm, close to the limit of nanofabrication techniques.

Once the photon magnetic field is known, the spin-photon coupling G^m in Eq. (3) can be calculated as follows:

$$G^m = \frac{g\mu_B}{\hbar}|\langle m|\mathbf{b} \cdot \mathbf{S}|m + 1\rangle|. \tag{8}$$

The direct relationship between the G^m and b suggests that, near a nanoconstriction, the spin-photon coupling can reach values much higher than those achieved for conventional resonators. Following this route, spin-photon couplings $G/2\pi$ near 1 kHz have been achieved experimentally for single spins 1/2 located close to a 45-nm constriction in a 1.5-GHz coplanar resonator [31], whereas $G/2\pi \simeq 3$ kHz was achieved with 8-GHz lumped-element resonators having 100-nm-wide inductors [32]. Figure 5(c) shows that working with very low-impedance resonators and sufficiently high frequencies (in this example, $\omega_r/2\pi = 7.5$ GHz) much higher values can be envisioned. The simulations give $G/2\pi \simeq 95$ kHz for a $S = 1/2$ qubit located near a 20-nm constriction in the inductor of the circuit shown in Fig. 5. Besides, and as discussed above, the coupling is also enhanced when working with high-spin molecules. The bottom and top panels in Fig. 6 correspond to spin qudits with easy-axis [$D < 0$ in Eq. (2)] and easy-plane ($D > 0$) magnetic anisotropy, respectively. It follows that the latter case, characterized by a ground state with $m = 0$, represents a more favorable situation. Then, single spin to single-photon couplings as large as 1 MHz can be achieved with a $S = 10$ molecule. A further enhancement could be obtained by proper choice of the molecule (e.g., with larger S) or by choosing peculiar eigenstates, such as atomic clock transition states $(|S\rangle \pm |-S\rangle)/\sqrt{2}$ [30,61]. Nonetheless, this value is already close to the physical limit for this approach, as it involves an optimum circuit design combined with a close to maximum photon confinement and a close to perfect integration of the molecules with the device.

The latter condition might at first look daunting. Molecules can be deposited from solution onto the circuits and then delivered to the region of the nanoconstrictions by an atomic force microscope [31] or by exploiting the tendency of some molecules to self-organize on surfaces [62–65]. Yet, depositing single molecules sufficiently close
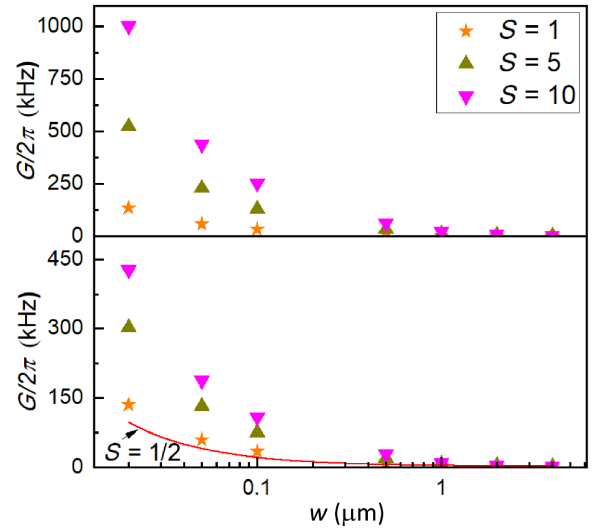

FIG. 6. Coupling to photons of individual spin qudits, located 1 nm above the inductor line of the LC resonator shown in Fig. 5(A). Results calculated for spins with easy axis [$D < 0$ in Eq. (2)] and easy plane ($D > 0$) are shown in, respectively, the bottom and top panels. They correspond to a different spin ground state and, therefore, to different resonant spin transitions. The solid line gives the coupling obtained for a simple $S = 1/2$ spin qubit.

to each constriction is very challenging and one will often end up having several molecules not too far apart. Nevertheless, we can address and manipulate individually each molecule (or each pair of molecules for two-qudit gates) by exploiting (i) the magnetic anisotropy [Eq. 2] and (ii) the strong dependence of the spin-photon coupling on the precise location [see Fig. 5(C)]. Indeed, in general we expect different molecules to deposit with a different orientation. Hence, only a specific one will meet the resonance condition required to implement both single- and two-qudit gates (as explained in Sec. II), while off-resonant ones will not undergo any evolution. Furthermore, a reduction of the coupling of at least one order of magnitude for molecules placed 50 nm apart from the nanoconstriction will practically forbid two-qudit gates (Sec. IIC) and make these spins undetectable (Sec. IID). Therefore, one can take advantage of the statistical nature of the molecular deposition processes and select those molecules from the ensemble that fulfill a given condition vis a vis a given circuit design. The molecular integration requisite then softens to having a sufficiently sparse surface coverage, which is achievable with molecular evaporation or self-organization techniques [63,65].

IV. NUMERICAL SIMULATIONS

Having introduced both the working principles and the realistic set of experimental conditions to operate the MSQP, we can now assess and quantify its performance

by numerical simulations. To this aim, we consider the full series of operations (i.e., classical pulses and variations of the resonator frequency) to implement sequences of one- and two-qudit gates in our platform. As in the previous discussion, we focus for simplicity on a elementary unit of the scalable setup, i.e., a single resonator containing a pair of qudits. Simulations are realized by numerically integrating the Lindblad equation for the full system density matrix ρ:

$$
\begin{aligned}
\dot{\rho} = &-i[H + H_1(t), \rho] \\
&+ \frac{1}{T_2} \sum_i \left(2S_{zi}\rho S_{zi} - S_{zi}^2\rho - \rho S_{zi}^2 \right) \\
&+ \frac{\omega_r}{2\pi Q} \left(2a\rho a^\dagger - a^\dagger a\rho - \rho a^\dagger a \right),
\end{aligned}
\tag{9}
$$

where the first line describes the coherent evolution, the second models pure dephasing (where we assume the same T_2 for the two qudits) and the last one represents photon loss. We assume in the following $G_i/2\pi \approx 90$ kHz (slightly different for the two spins to better match experimental conditions), in line with the best values reported in Fig. 5, and $\omega_0/2\pi = 7.5$ GHz. This choice yields $G_i^0/2\pi \approx 1$ MHz for transitions involved in two-qubit gates reported below. As far as the spin system is concerned, we use $D_1/2\pi = 7.1$ GHz, $D_2/2\pi = 7.7$ GHz, $g_i = 2$, $B = 50$ mT. The small static field is compatible with superconducting circuitry technology. Below we first report simulations of single-qudit operations, using classical driving fields to implement the Deutsch algorithm on a four-level qudit as illustrated in Sec. II B. We then quantify and compare the performance of two-qubit entangling gates such as the controlled-Z and iSWAP gates described above, employing the resonant and dispersive approaches, respectively. We finally focus on specific applications such as quantum simulation, in which several one- and two-qubit gates are concatenated.

A. Multiqubit algorithms onto a single qudit

Hereafter we exploit the four lowest energy states of qudit 1 to encode two qubits and we show how to decompose the two-qubit Deutsch-Jozsa (DJ) algorithm [66] into a sequence of planar rotations on the qudit. The aim of this algorithm is to determine if a given function, f, is either constant or balanced. The algorithm implements the transformation $|x\rangle_q|y\rangle_a \rightarrow |x\rangle_q|y \oplus f(x)\rangle_a$ producing $|0\rangle_q$ as the final state for the input qubit if f is constant and $|1\rangle_q$ otherwise. Here $|\ \rangle_{q(a)}$ denotes the state of the input (ancilla) qubit and the sum is a mod(2) addition. The constant functions that we are going to implement are $U_{f_1} = \mathbb{I}^{\otimes 2}$ and $U_{f_2} = \mathbb{I}_q \otimes X_a$ and $U_{f_3} = CX_{q \rightarrow a}$, $U_{f_4} = X_q CX_{q \rightarrow a} X_q$ are the balanced ones. Here $CX_{q \rightarrow a}$ is a controlled-NOT gate where q acts as a control on a. Following the procedure detailed in Sec. II B, we map the following levels from our qudit $\{|m\rangle\} = \{|0\rangle, |+1\rangle, |-$

$1\rangle, |-2\rangle\} \equiv \{|0\rangle, |1\rangle, |2\rangle, |3\rangle\}$ to the multiqubit ones: $\{|0\rangle, |1\rangle, |2\rangle, |3\rangle\} \equiv \{|0\rangle_q|0\rangle_a, |0\rangle_q|1\rangle_a, |1\rangle_q|0\rangle_a, |1\rangle_q|1\rangle_a\}$. With this relation, we can now proceed to decompose the multiqubit circuit into the exact sequence of pulses that have to be applied to our molecule to implement the full algorithm, which is shown schematically in Fig. 7(a). It is worthwhile to notice that the levels chosen from our molecule do not have the ideal ladder connectivity since the states $|1\rangle$ and $|2\rangle$ are not connected directly. This is solved by adding a $|0\rangle \rightarrow |1\rangle$ gate to the $|0\rangle \rightarrow |2\rangle$ rotation. The operations that appear as arrows in Fig. 7(a) represent the different pulses to be applied: the color indicates the axis direction and the parameter in brackets the rotation angle (parameters ϕ and θ in Eq. (5), respectively). Recall that rotations around the z axis can be implemented from the other two axis rotations [cf. Sec. II B]. With this we now evolve the system integrating Eq. (9) for different values of the driving magnetic field, B_1, and of the decoherence time, T_2, to compute the error committed in the implementation. In the qubit case one expects to get the state $|0\rangle_q$ ($|1\rangle_q$) for a constant (balanced) function. In the qudit case, with this encoding, measuring $|0\rangle_q$ ($|1\rangle_q$) corresponds to a projection onto the subspace spanned by the states $\{|0\rangle, |1\rangle\}$ ($\{|2\rangle, |3\rangle\}$). Therefore, to evaluate the performance of our implementation, we compute the error as $\mathcal{E} = Tr(\rho P)$, being ρ the final state obtained from the pulse sequence and P the projector onto the "wrong" subspace, i.e., $P = |0\rangle\langle 0| + |1\rangle\langle 1|$ for U_{f_3} and U_{f_4}; $P = |2\rangle\langle 2| + |3\rangle\langle 3|$ for U_{f_1} and U_{f_2}. Figure 7 (b) shows that the error is clearly reduced by increasing T_2 and reaches values of the order of 1 %. Increasing B_1 has the effect of speeding up the gates, thus reducing the effect of dephasing. However, increasing it too much can worsen the results due to leakage effects.

B. Two-qudit gates

We now investigate the implementation of a two-qudit controlled-Z gate according to our alternative resonant approach, between a two- and a four-level qudit (plus an auxiliary level $|e\rangle$ used during the gate), as in the scheme of Fig. 2. As figures of merit for the performance of the gate, we consider here the fidelity $\mathcal{F} = \langle \psi | \rho | \psi \rangle$, which quantifies the overlap between the desired state $|\psi\rangle$ that one gets in an ideal implementation of the gate and the actual state ρ obtained by solving Eq. (9). As a benchmark, we consider a particularly error-prone initial state, in which all the components in the computational basis are populated (randomly) with significant weight (see caption of Fig. 8).

Figure 8 shows a colormap of the resulting error $\mathcal{E} = 1 - \mathcal{F}$ as a function of the resonator quality factor Q and of the qudits coherence time T_2. The error is clearly reduced both by increasing Q and T_2, but it shows a stronger dependence on the qudit coherence time. In particular, Q values above 10^6 give only a minor improvement, while
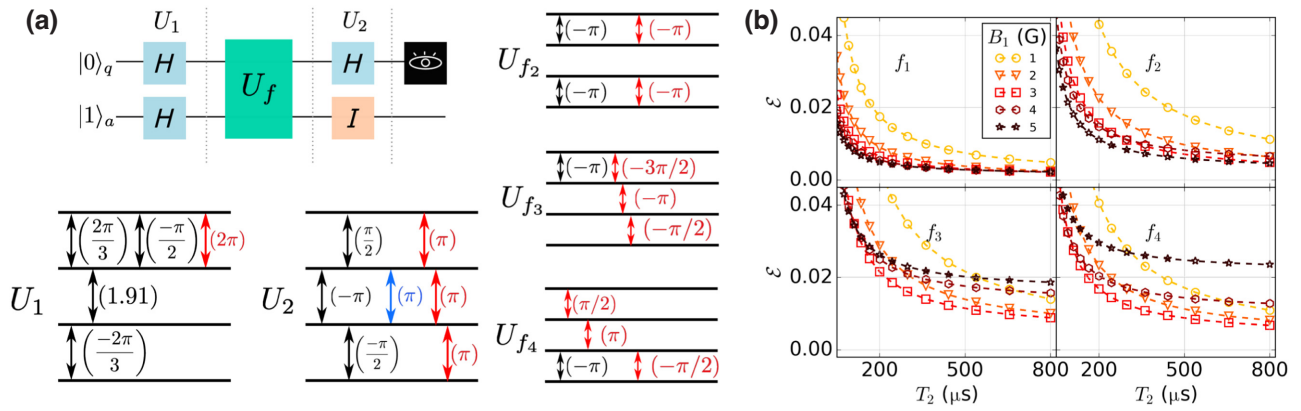
FIG. 7. Decomposition of the circuit for the Deutsch-Jozsa (two-qubit) algorithm into a sequence of pulses on a four-level qudit. (a) Schematic representation of the two-qubit circuit and of the sequence of qudit operations needed to implement each unitary. Each arrow color represents one rotation direction [parameter ϕ in Eq. (5)]: black for Y, blue for X, and red for Z. (b) Error dependence with the driving magnetic field, B_1, and with the decoherence time T_2. The error is computed as $\mathcal{E} = Tr(\rho P)$ and P is the projector onto the subspace in which the final wave function must not be contained according to the applied function, U_{f_i}.

$\mathcal{F}$ smoothly increases with T_2 even in the ms range. Nevertheless, the fidelity already overcomes 99 % for $T_2 = 400$ μs. This is made even more evident by considering the T_2 dependence of the fidelity, shown in Fig. 9 for different values of Q.

As a comparison, here we also report simulations of the iSWAP gate in the dispersive regime, where we assume $\Delta_1/2\pi = 20$ MHz, $\Delta_2/2\pi = 30$ MHz for the lowest-energy transitions of the two spins in the idle configuration. These are then tuned into mutual resonance ($\Delta_1 = \Delta_2 = 20$ MHz $\times 2\pi$) to activate the iSWAP. In this configuration, $\Delta_1 \approx 20\, G_i^0$ and hence we are safely in the dispersive

regime, with negligible leakage to the excited one-photon states.

We first note that the fidelity of the iSWAP gate is practically independent of Q, in contrast to the resonant case. This was expected, because of the virtual versus real exchange of photons in the two methods. However, the approximately 6 times larger value of τ_{2q} for implementing the iSWAP compared to the controlled Z makes the iSWAP more prone to decoherence, resulting in a significantly lower fidelity, only approaching that of the controlled Z at very long T_2.
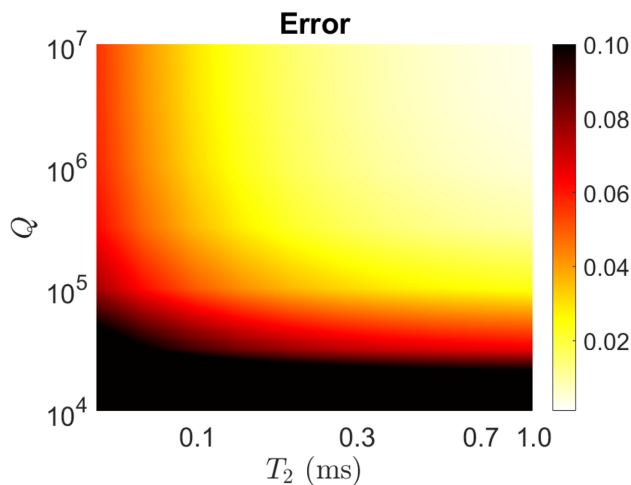

FIG. 8. Error $1 - \mathcal{F}$ (log scale) in the implementation of the resonant controlled-Z gate as a function of the resonator quality factor Q and of the qudits' coherence time T_2. Random components on $|p\rangle |q\rangle$ initial state are given by $|0\rangle |q\rangle = (0.31, 0.46, 0.48, 0.37)$ and $|1\rangle |q\rangle = (0.37, 0.25, 0.25, 0.24)$ with $q = 0, 1, 2, 3$.
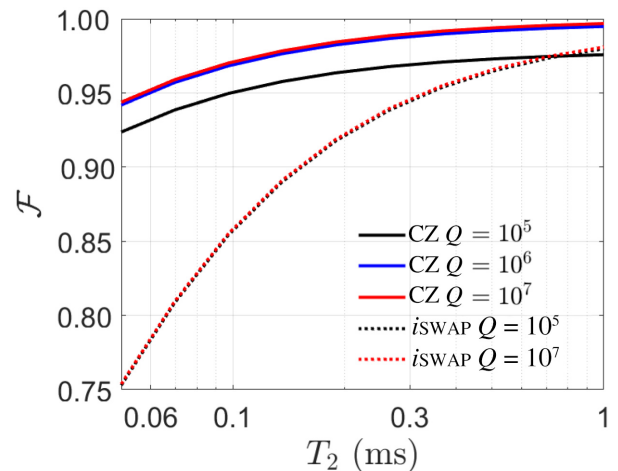

FIG. 9. Fidelity in the implementation of the controlled-Z (CZ) gate in the resonant regime (solid lines) and of the iSWAP gate in the dispersive regime (dotted) as a function of the qudits' coherence time T_2, for different values (colors) of the resonator quality factor Q.

C. Application: quantum simulation

To better highlight the difference between the resonant and dispersive approach in implementing a conditional two-qudit dynamics, we consider here a specific application of the gates described above. Indeed, different gates can be targeted to different goals. Therefore, depending on the specific algorithm, a more efficient decomposition can be found by exploiting either *i*SWAP or controlled-*Z* gates. A clear comparison can be made by considering the quantum simulation of the Heisenberg model, which can be decomposed by exploiting an equal number of controlled-phase or $U_{XY}(\tau)$ gates. In particular, our aim is to simulate the dynamics associated to the target Hamiltonian

$$\mathcal{H}_H = J \left(s_{x,1}s_{x,2} + s_{y,1}s_{y,2} + s_{z,1}s_{z,2} \right), \quad (10)$$

where $s_{\alpha,i}$ are spin-1/2 operators. Performing a quantum simulation corresponds to implement the unitary $U(Jt) = e^{-i\mathcal{H}_H t}$, starting from a generic state. In the present case, the three terms in Eq. (10) commute, and hence we can reproduce the dynamics of $U(Jt)$ by subsequently implementing the three unitaries $U_{\alpha\alpha}(Jt) = \exp\left[-iJts_{\alpha,1}s_{\alpha,2}\right]$ for $\alpha = x, y, z$. These can be obtained by combining either the controlled phase (U_φ) or the $U_{XY}(\tau)$ with proper single-qubit rotations.

As far as the resonant controlled phase is concerned, we start from $U_{zz}(Jt)$. This can be easily rewritten in terms of controlled-phase gates and single-qubit rotations [41], i.e., $U_{zz}(\varphi) \propto e^{i\varphi/2} U_\varphi^{11} R_z(\varphi/2)$. Here $R_z(\varphi)$ are single-qubit rotations about the z axis of an angle φ on both qubits. By setting $\varphi = Jt$ we simulate the target $U_{zz}(Jt)$. The latter can be easily transformed into $U_{xx}(Jt)$ by a simple change of reference frame, i.e., $U_{xx}(Jt) = R_y(\pi/2)U_{zz}(Jt)R_y(-\pi/2)$ and analogously for $U_{yy}(Jt)$. Overall, we need three controlled-phase gates and five rotations (on both qubits) to simulate the Heisenberg model.

Following instead the dispersive approach, $U_{XY}(\tau)$ is naturally mapped into $U_{xx}U_{yy}$. Then, we can exploit again changes of reference frame to transform this into $U_{xx}U_{zz}$ (by means of $R_x(\pm\pi/2)$ rotations) or into $U_{yy}U_{zz}$ [via $R_y(\pm\pi/2)$]. By concatenating these three steps we get $U(Jt) = U_{zz}(Jt/2)U_{yy}(Jt/2)U_{xx}(Jt/2)U_{zz}(Jt/2)U_{xx}(Jt/2)$ $U_{yy}(Jt/2)$ [67,68]. Also in this case, the Heisenberg evolution is obtained by using three two-qubit gates $U_{XY}(\tau)$ and four single-qubit rotations. Hence, this is a very good benchmark to compare the two methods.

To perform the quantum simulation, we exploit the two lowest energy levels of both qudits in the processor as logical states and the third one on q_1 as an auxiliary state for the implementation of the controlled-phase gate [see Sec. II C]. Results of our simulations following the two different approaches are shown in Fig. 10, where we plot the time evolution of the expectation values of s_{z1} (red) and s_{z2} (black). First, it is worth noting that the resonant approach gives optimal results already for $T_2 = 50\,\mu$s, in the whole
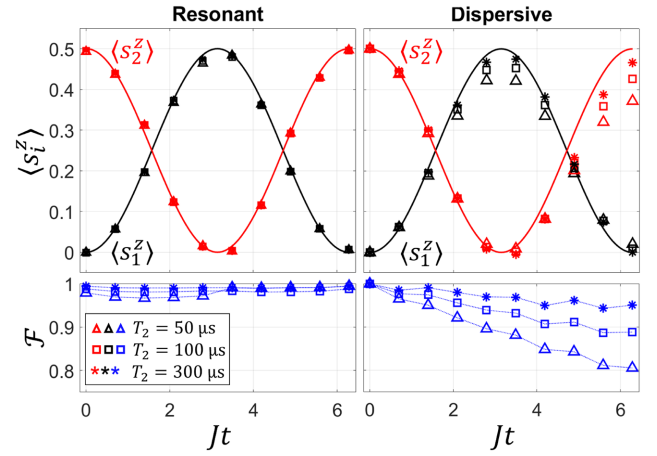

FIG. 10. Comparison between resonant (left) and dispersive (right) approaches in the digital quantum simulation of the Heisenberg model, and associated fidelity (bottom panels) as a function of the simulated time. The system is initialized in $(|00\rangle + |01\rangle)/\sqrt{2}$. In the top panels we report the time evolution of the expectation values of s_{z1} (red) and s_{z2} (black). The resonator quality factor is fixed to $Q = 10^6$.

range of simulation times t. Then, while for short t the accuracy of the two methods (and the associated fidelity, lower panels) is similar, the performance of the dispersive approach breaks down as long as Jt increases. Conversely, the resonant method displays a fidelity which is practically independent of Jt. This behavior can be easily understood by considering that Jt is associated either to the angle φ of the controlled phase or to the time evolution τ of the $U_{XY}(\tau)$ gate. While the duration of the controlled phase is only weakly dependent on φ, the duration of $U_{XY}(\tau)$ increases linearly with τ. As a consequence, in the resonant regime the simulation lasts approximately 3 μs independently of the simulated time, while in the dispersive regime it increases up to 17 μs at $Jt = 2\pi$, thus giving reliable results only for T_2 of hundreds of μs.

Having demonstrated the general better performance of the resonant approach, we now consider its application to another, more difficult problem represented by the quantum simulation of the transverse-field Ising model (TIM). The target Hamiltonian on a chain of N spins 1/2 is given by

$$\mathcal{H}_T = J \sum_{i=1}^{N-1} s_{z,i}s_{z,i+1} + b \sum_{i=1}^{N} s_{x,i}. \quad (11)$$

The associated dynamics is nontrivial and gives rise to a quantum phase transition for specific values of the parameters J and b. In the present case, the two noncommuting terms in Hamiltonian (11), namely $\mathcal{H}_1 = b \sum_{i=1}^{N} s_{x,i}$ and
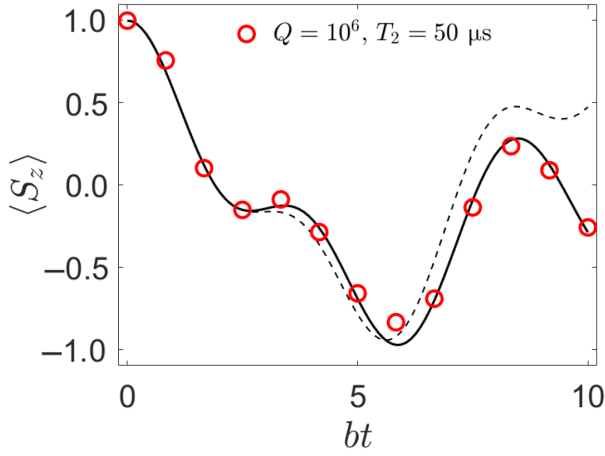
FIG. 11.   Quantum simulation of the time evolution of the system magnetisation $\langle S_z \rangle \equiv \langle s_{z,1} + s_{z,2} \rangle$ for the transverse-field Ising model on two qubits. Dashed (continuous) line represents the exact evolution (after Trotter decomposition, $n = 6$). Colored points are the results of full numerical simulation, including the effect of photon loss, parametrized by the resonator quality factor Q, and of spin pure dephasing, parametrized by the coherence time T_2.

$\mathcal{H}_2 = J \sum_{i=1}^{N-1} s_{z,i} s_{z,i+1}$, require a Suzuki-Trotter decomposition to approximate the unitary U, i.e.,

$$U = e^{-i\mathcal{H}_T t} \approx \left(e^{-i\mathcal{H}_1 t/n} e^{-i\mathcal{H}_2 t/n} \right)^n. \qquad (12)$$

Here n is the number of Suzuki-Trotter steps in the decomposition, the first (one-body) term directly corresponds to single-qubit rotations $e^{-i\mathcal{H}_1 t/n} \equiv R_x(bt/n)$ on the whole register, while the second is obtained as described above. For our benchmark, we focus on a two-qubit system ($N = 2$) in the most demanding regime $J = 2b$, where the commutator between the two terms in the target Hamiltonian (11) $[\mathcal{H}_1, \mathcal{H}_2]$ is the largest and hence a large number of Suzuki-Trotter steps is required for a reliable quantum simulation.

Results of our numerical simulations are reported in Fig. 11, using $n = 6$ Trotter steps. This corresponds to a sequence of n controlled phase gates (implemented by variations of the resonator frequency, as illustrated in Sec. II.C) and $2n$ rotations (implemented via classical drives). To compare the results of our simulation with the expected ones, we compute the final magnetization of the target system $\langle S_z(t) \rangle = \langle \psi(t)| s_{z,1} + s_{z,2} |\psi(t) \rangle$, where $|\psi(t)\rangle = U|\psi_0\rangle$ is the target system state at the simulated time t and $|\psi_0\rangle = |00\rangle$.

In spite of the significant number of operations (12 rotations and six controlled-phase gates) involved in the quantum simulation of each point in Fig. 11, the MSQP is able to reproduce very well the expected behavior of $\langle S_z \rangle$, even with $Q = 10^6$ and $T_2 = 50$ μs.

V. DISCUSSION AND CONCLUSIONS

We introduce the working principles of a quantum processing unit based on molecular nanomagnets coupled to superconducting circuits, and test its performance via numerical simulations based on a realistic experimental layout. The results are promising and indicate that the MSQP designed in this work traces a viable path for manipulating individual molecular qudits and for wiring them up in a scalable device. In particular, we exploit the hybrid character of the proposed architecture that combines the mobility of photons to the multilevel structure of spin systems. This allows one to implement entangling gates even between distant molecules in the register with no need of highly demanding SWAP operations, and to switch off completely their coupling at the end of the gate, thus avoiding crucial cross-talking issues, which occur in the presence of a permanent qubit-qubit interaction [20].

The simulations achieve a high fidelity in the implementation of two-qudit gates in the resonant regime, by using spin coherence times of a few hundreds of μs. These results represent a key improvement compared to the dispersive regime, thanks to the significant speedup achieved in the implementation of entangling gates. A drawback of the resonant approach (which is however strongly limited by encoding logical states in $n_{\text{ph}} = 0$ subspace) is represented by photon loss, whose effect is instead practically negligible for the dispersive method. To mitigate these issues, intermediate regimes (with detuning of the order of approximately $5 \, G_i^m$) could be explored. Although less flexible (the time evolution of $U_{XY}(\tau)$ should be limited to fixed values of τ to avoid leakage), this would allow for reaching gating times similar to the resonant case, with a reduced effect of photon loss.

Moreover, to solve specific problems (e.g., quantum simulation) the MSQP could already operate with good performance even with significantly shorter values of $T_2 \sim$ tens of μs. These values have already been achieved and even largely overcome in molecular spin qubits [15,17], in much worse experimental conditions than those proposed here, i.e., at significantly higher temperatures and on a (diluted) molecular ensemble. The possibility to reach these T_2 with qudits needs still to be experimentally investigated, although theoretical results indicate that optimal coherence could be obtained in compounds with the suitable pattern of interactions [35,38].

Further improvements could be obtained by enhancing the ratio T_2/τ_{2q} between coherence and gate times. This, in turn, calls for a joint multidisciplinary effort to increase not only spin coherence but also the coupling of spins to superconducting resonators. Increasing the values estimated under Sec. III by pushing the circuit miniaturization is a challenge, although the application of ultrahigh resolution nanolithography methods might still provide room for some improvement [69]. The alternative is to look

for a different coupling regime between spins and photons. A possibility is to introduce interaction mediators based on magnonic excitations [70,71], e.g., in magnetic films or two-dimensional materials, investigate the coupling of spins with electric instead of magnetic fields (as recently done in an EPR setup [72–74]) or even explore hybrid circuits that might bring tools from molecular electronics [75–77] into the circuit-QED realm. In parallel to seeking alternative circuit designs, the spin-photon coupling could also be improved via a proper engineering of the system Hamiltonian. For instance, a further factor of approximately 2 in the effective coupling could be reached by encoding qubits into atomic clock transition states $(|S\rangle \pm |-S\rangle)/\sqrt{2}$, coupled by S_z and protected from magnetic field fluctuations.

On the chemical side, different classes of compounds could be explored. Besides multispin clusters with very large total spin ground state [48], other possible implementations are offered by lanthanide qubits, whose g tensors can be engineered to achieve values up to 5–10 [37] and hence a corresponding enhancement of the spin-photon coupling. For instance, Yb(trensal) complex [12] shows $g_z = 4.3$ and ensembles of this molecule have already been coupled to superconducting resonators [33].

All these classes of compounds share the typical trademark of MNMs, i.e., they provide many low-energy states, which represent a crucial resource to simplify quantum algorithms and especially to embed quantum error correction. By combining this peculiar advantage with an accurate design of the device, we indicate here a clear route for the actual realization of a promising kind of quantum chip. Indeed, integration of molecular spins, offering advantages as multilevel logical units, into existing superconducting resonators takes advantages from both classes of materials and bridges the gap between current and future technologies.

[1] F. Tacchino, A. Chiesa, S. Carretta, and D. Gerace, Quantum computers as universal quantum simulators: State-of-the-art and perspectives, Adv. Quantum Technol. **3**, 1900052 (2019).

[2] G. N. Nop, D. Paudyal, and J. D. H. Smith, Ytterbium ion trap quantum computing: The current state-of-the-art, AQS **3**, 044101 (2021).

[3] F. Arute *et al.*, Hartree-Fock on a superconducting qubit quantum computer, Science **369**, 1084 (2020).

[4] F. Arute *et al.*, Quantum supremacy using a programmable superconducting processor., Nature **574**, 505 (2019).

[5] P. Jurcevic *et al.*, Demonstration of quantum volume 64 on a superconducting quantum computing system, Quantum Sci. Technol. **6**, 025020 (2021).

[6] I. Pogorelov, T. Feldker, C. D. Marciniak, L. Postler, G. Jacob, O. Krieglsteiner, V. Podlesnic, M. Meth, V. Negnevitsky, M. Stadler, B. Höfer, C. Wächter, K. Lakhmanskiy, R. Blatt, P. Schindler, and T. Monz, Compact Ion-Trap Quantum Computing Demonstrator, PRX Quantum **2**, 020343 (2021).

[7] P. D. Nation, H. Kang, N. Sundaresan, and J. M. Gambetta, Scalable Mitigation of Measurement Errors on Quantum Computers, PRX Quantum **2**, 040326 (2021).

[8] C. Piveteau, D. Sutter, S. Bravyi, J. M. Gambetta, and K. Temme, Error Mitigation for Universal Gates on Encoded Qubits, Phys. Rev. Lett. **127**, 200505 (2021).

[9] Y.-M. Di and H.-R. Wei, Optimal synthesis of multivalued quantum circuits, Phys. Rev. A **92**, 062317 (2015).

[10] F. Tacchino, A. Chiesa, R. Sessoli, I. Tavernelli, and S. Carretta, A proposal for using molecular spin qudits as quantum simulators of light–matter interactions, J. Mater. Chem. C **9**, 10266 (2021).

[11] M. H. Michael, M. Silveri, R. Brierley, V. V. Albert, J. Salmilehto, L. Jiang, and S. M. Girvin, New Class of Quantum Error-Correcting Codes for a Bosonic Mode, Phys. Rev. X **6**, 031006 (2016).

[12] R. Hussain, G. Allodi, A. Chiesa, E. Garlatti, D. Mitcov, A. Konstantatos, K. Pedersen, R. D. Renzi, S. Piligkos, and S. Carretta, Coherent manipulation of a molecular ln-based nuclear qudit coupled to an electron qubit, J. Am. Chem. Soc. **140**, 9814 (2018).

[13] A. Chiesa, E. Macaluso, F. Petiziol, S. Wimberger, P. Santini, and S. Carretta, Molecular nanomagnets as qubits with embedded quantum-error correction, J. Phys. Chem. Lett. **11**, 8610 (2020).

[14] S. Carretta, D. Zueco, A. Chiesa, A. Gómez-León, and F. Luis, A perspective on scaling up quantum computation with molecular spins, Appl. Phys. Lett. **118**, 240501 (2021).

[15] J. M. Zadrozny, J. Niklas, O. G. Poluektov, and D. E. Freedman, Millisecond coherence time in a tunable molecular electronic spin qubit, ACS Cent. Sci. **1**, 488 (2015).

[16] M. Atzori, L. Tesi, E. Morra, M. Chiesa, L. Sorace, and R. Sessoli, Room-temperature quantum coherence and Rabi oscillations in Vanadyl phthalocyanine: Toward multifunctional molecular spin qubits, J. Am. Chem. Soc. **138**, 2154 (2016).

[17] K. Bader, D. Dengler, S. Lenz, B. Endeward, S.-D. Jiang, P. Neugebauer, and J. van Slageren, Room temperature quantum coherence in a potential molecular qubit, Nat. Commun. **5**, 5304 (2014).

[18] Y.-S. Ding, Y.-F. Deng, and Y.-Z. Zheng, The rise of single-ion magnets as spin qubits, Magnetochemistry **2**, 40 (2016).

[19] A. Ardavan, A. M. Bowen, A. Fernandez, A. J. Fielding, D. Kaminski, F. Moro, C. A. Muryn, M. D.Wise, A. Ruggi, E. J. L. McInnes, Kay Severin, Grigore A. Timco, Christiane R. Timmel, Floriana Tuna, George F. S. Whitehead, and Richard E. P. Winpenny, Engineering coherent interactions in molecular nanomagnet dimers, Npj Quantum Inf. **1**, 15012 (2015).

[20] J. Ferrando-Soria, E. Moreno-Pineda, A. Chiesa, A. Fernandez, S. A. Magee, S. Carretta, P. Santini, I. Vitorica-Yrezabal, F. Tuna, E. J. L. McInness, and R. E. P. Winpenny, A modular design of molecular qubits to implement universal quantum gates, Nat. Commun. **7**, 11377 (2016).

[21] M. Atzori, A. Chiesa, E. Morra, M. Chiesa, L. Sorace, S. Carretta, and R. Sessoli, A two-qubit molecular architecture for electronmediated nuclear quantum simulation, Chem. Sci. **9**, 6183 (2018).

[22] S. J. Lockyer, A. Chiesa, A. Brookfield, G. A. Timco, G. F. S. Whitehead, E. J. L. McInnes, S. Carretta, and R. E. P. Winpenny, Five-spin supramolecule for simulating quantum decoherence of Bell states, J. Am. Chem. Soc **144**, 16086 (2022).

[23] C. J. Rogers, D. Asthana, A. Brookfield, A. Chiesa, G. A. Timco, D. Collison, L. S. Natrajan, S. Carretta, R. E. P. Winpenny, and A. M. Bowen, Modelling conformational flexibility in a spectrally addressable molecular multi-qubit model system, Angew. Chem. Int. Ed **61**, e202207947 (2022).

[24] S. Chicco, A. Chiesa, G. Allodi, E. Garlatti, M. Atzori, L. Sorace, R. De Renzi, R. Sessoli, and S. Carretta, Controlled coherent dynamics of [VO(TPP)], a prototype molecular nuclear qudit with an electronic ancilla, Chem. Sci. **12**, 12046 (2021).

[25] M. Atzori, E. Garlatti, G. Allodi, S. Chicco, A. Chiesa, A. Albino, R. D. Renzi, E. Salvadori, M. Chiesa, S. Carretta, and L. Sorace, Radiofrequency to microwave coherent manipulation of an organometallic electronic spin qubit coupled to a nuclear qudit, Inorg. Chem. **60**, 11273 (2021).

[26] A. Blais, R.-S. Huang, A. Wallraff, S. M. Girvin, and R. J. Schoelkopf, Cavity quantum electrodynamics for superconducting electrical circuits: An architecture for quantum computation, Phys. Rev. A **69**, 062320 (2004).

[27] A. Wallraff, D. I. Schuster, A. Blais, L. Frunzio, R.-S. Huang, J. Majer, S. Kumar, S. M. Girvin, and R. J. Schoelkopf, Strong coupling of a single photon to a superconducting qubit using circuit quantum electrodynamics, Nature **431**, 162 (2004).

[28] J. Majer, J. M. Chow, J. M. Gambetta, J. Koch, B. R. Johnson, J. A. Schreier, L. Frunzio, D. I. Schuster, A. A. Houck, A. Wallraff, A. Blais, M. H. Devoret, S. M. Girvin, and R. J. Schoelkopf, Coupling superconducting qubits via a cavity bus, Nature **449**, 443 (2007).

[29] R. J. Schoelkopf and S. M. Girvin, Wiring up quantum systems, Nature **451**, 664 (2008).

[30] M. D. Jenkins, D. Zueco, O. Roubeau, G. Aromí, J. Majer, and F. Luis, A scalable architecture for quantum computation with molecular nanomagnets, Dalton Trans. **45**, 16682 (2016).

[31] I. Gimeno, W. Kersten, M. C. Pallarés, P. Hermosilla, M. J. Martínez-Pérez, M. D. Jenkins, A. Angerer, C. Sánchez-Azqueta, D. Zueco, J. Majer, A. Lostao, and F. Luis, Enhanced molecular spin-photon coupling at superconducting nanoconstrictions, ACS Nano **14**, 8707 (2020).

[32] V. Ranjan, S. Probst, B. Albanese, T. Schenkel, D. Vion, D. Esteve, J. J. L. Morton, and P. Bertet, Electron spin resonance spectroscopy with femtoliter detection volume, Appl. Phys. Lett **116**, 184002 (2020).

[33] V. Rollano, M. C. de Ory, C. D. Buch, M. Rubín-Osanz, D. Zueco, C. Sánchez-Azqueta, A. Chiesa, D. Granados, S. Carretta, A. Gomez, S. Piligkos, and F. Luis, High cooperativity coupling to nuclear spins on a circuit quantum electrodynamics architecture, Commun. Phys. **5**, 246 (2022).

[34] C. Bonizzoni, M. Maksutoglu, A. Ghirri, J. van Tol, B. Rameev, and M. Affronte, Coupling sub-nanoliter BDPA organic radical spin ensembles with YBCO inverse anapole resonators, Appl. Magn. Reson. **54**, 143 (2023).

[35] A. Chiesa, F. Petiziol, M. Chizzini, P. Santini, and S. Carretta, Theoretical design of optimal molecular qudits for quantum error correction, J. Phys. Chem. Lett **13**, 6468 (2022).

[36] M. Chizzini, L. Crippa, A. Chiesa, F. Tacchino, F. Petiziol, I. Tavernelli, P. Santini, and S. Carretta, Molecular nanomagnets with competing interactions as optimal units for qudit-based quantum computation, Phys. Rev. Res. **4**, 043135 (2022).

[37] E. Macaluso, M. Rubín, D. Aguilà, A. Chiesa, J. I. M. L. A. Barrios, P. J. Alonso, O. Roubeau, F. Luis, G. Aromí, and S. Carretta, A heterometallic [LnLn'Ln] lanthanide complex as a qubit with embedded quantum error correction, Chem. Sci. **11**, 10337 (2020).

[38] F. Petiziol, A. Chiesa, S. Wimberger, P. Santini, and S. Carretta, Counteracting dephasing in molecular nanomagnets by optimized qudit encodings, Npj Quantum Inf. **7**, 133 (2021).

[39] M. Chizzini, L. Crippa, L. Zaccardi, E. Macaluso, S. Carretta, A. Chiesa, and P. Santini, Quantum error correction with molecular spin qudits, Phys. Chem. Chem. Phys. **24**, 20030 (2022).

[40] S. Carretta, A. Chiesa, F. Troiani, D. Gerace, G. Amoretti, and P. Santini, Quantum Information Processing with Hybrid Spin-Photon Qubit Encoding, Phys. Rev. Lett. **111**, 110501 (2013).

[41] A. Chiesa, P. Santini, D. Gerace, J. Rafter, A. A. Houck, and S. Carretta, Digital quantum simulators in a scalable architecture of hybrid spin-photon qubits, Sci. Rep. **5,** 16036 (2015).

[42] A. Palacios-Laloy, F. Nguyen, F. Mallet, P. Bertet, D. Vion, and D. Esteve, Tunable resonators for quantum circuits, J. Low Temp. Phys. **151,** 1034 (2008).

[43] A. Gómez-León, Multiqudit interactions in molecular spins, Phys. Rev. A **106,** 022609 (2022).

[44] R. Caciuffo, G. Amoretti, A. Murani, R. Sessoli, A. Caneschi, and D. Gatteschi, Neutron Spectroscopy for the Magnetic Anisotropy of Molecular Clusters, Phys. Rev. Lett. **81,** 4744 (1998).

[45] A. L. Barra, D. Gatteschi, and R. Sessoli, High-frequency epr spectra of a molecular nanomagnet: Understanding quantum tunneling of the magnetization, Phys. Rev. B **56,** 8192 (1997).

[46] A. Chiesa, T. Guidi, S. Carretta, S. Ansbro, G. A. Timco, I. Vitorica-Yrezabal, E. Garlatti, G. Amoretti, R. E. P. Winpenny, and P. Santini, Magnetic Exchange Interactions in the Molecular Nanomagnet mn$_{12}$, Phys. Rev. Lett. **119,** 217202 (2017).

[47] D. Collison, M. Murrie, V. S. Oganesyan, S. Piligkos, N. R. J. Poolton, G. Rajaraman, G. M. Smith, A. J. Thomson, G. A. Timko, W. Wernsdorfer, R. E. P. Winpenny, and E. J. L. McInnes, Magnetic and optical studies on an $S = 6$ ground-state cluster $[Cr_12O_9(OH)_3(O_2CCMe_3)15]$: Determination of, and the relationship between, single-ion and cluster spin Hamiltonian parameters, Inorg. Chem. **42,** 5293 (2003).

[48] O. Waldmann, A. M. Ako, H. U. Güdel, and A. K. Powell, Assessment of the anisotropy in the molecule Mn$_{19}$ with a high-spin ground state $S = 83/2$ by 35 GHz electron paramagnetic resonance, Inorg. Chem. **47,** 3486 (2008).

[49] G. K. Brennen, D. P. O'Leary, and S. S. Bullock, Criteria for exact qudit universality, Phys. Rev. A **71,** 052318 (2005).

[50] A. Castro, A. García Carrizo, S. Roca, D. Zueco, and F. Luis, Optimal Control of Molecular Spin Qudits, Phys. Rev. Appl. **17,** 064028 (2022).

[51] D. Zueco, G. M. Reuther, S. Kohler, and P. Hänggi, Qubit-oscillator dynamics in the dispersive regime: Analytical theory beyond the rotating-wave approximation, Phys. Rev. A **80,** 033846 (2009).

[52] Z. L. Wang, Y. P. Zhong, L. J. He, H. Wang, J. M. Martinis, A. N. Cleland, and Q. W. Xie, Quantum state characterization of a fast tunable superconducting resonator, Appl. Phys. Lett. **102,** 163503 (2013).

[53] A. Gómez-León, F. Luis, and D. Zueco, Dispersive Readout of Molecular Spin Qudits, Phys. Rev. Appl. **17,** 064030 (2022).

[54] T. Walter, P. Kurpiers, S. Gasparinetti, P. Magnard, A. Potočnik, Y. Salathé, M. Pechal, M. Mondal, M. Oppliger, C. Eichler, and A. Wallraff, Rapid High-Fidelity Single-Shot Dispersive Readout of Superconducting Qubits, Phys. Rev. Appl. **7,** 054020 (2017).

[55] J. Wang, F. Sciarrino, A. Laing, and M. G. Thompson, Integrated photonic quantum technologies, Nat. Photon. **14,** 273 (2020).

[56] M. Atzori, E. Morra, L. Tesi, A. Albino, M. Chiesa, L. Sorace, and R. Sessoli, Quantum coherence times enhancement in vanadium(IV)-based potential molecular qubits: The key role of the vanadyl moiety, J. Am. Chem. Soc. **138,** 11234 (2016).

[57] D. L. Underwood, W. E. Shanks, J. Koch, and A. A. Houck, Low-disorder microwave cavity lattices for quantum simulation with photons, Phys. Rev. A **86,** 023837 (2012).

[58] A. Megrant, C. Neill, R. Barends, B. Chiaro, Y. Chen, L. Feigl, J. Kelly, E. Lucero, M. Mariantoni, P. J. J. O'Malley, D. Sank, A. Vainsencher, J. Wenner, T. C. White, Y. Yin, J. Zhao, C. J. Palmstrøm, John M. Martinis, and A. N. Cleland, Planar superconducting resonators with internal quality factors above one million, Appl. Phys. Lett. **100,** 113510 (2012).

[59] Sonnet Software Inc., Sonnet user's guide, release 18. [online].

[60] M. M. Khapaev, M. Y. Kupriyanov, E. Goldobin, and M. Siegel, Current distribution simulation for superconducting multi-layered structures, Supercond Sci Technol **16,** 24 (2002).

[61] M. Jenkins, T. Hümmer, M. J. Martínez-Pérez, J. García-Ripoll, D. Zueco, and F. Luis, Coupling single-molecule magnets to quantum circuits, New. J. Phys **15,** 095007 (2013).

[62] N. Domingo, E. Bellido, and D. Ruiz-Molina, Advances on structuring, integration and magnetic characterization of molecular nanomagnets on surfaces and devices, Chem. Soc. Rev. **41,** 258 (2012).

[63] G. Serrano, L. Poggini, M. Briganti, A. L. Sorrentino, G. Cucinotta, L. Malavolti, B. Cortigiani, E. Otero, P. Sainctavit, S. Loth, Francesca Parenti, Anne-Laure Barra, Alessandro Vindigni, Andrea Cornia, Federico Totti, Matteo Mannini, and Roberta Sessoli, Quantum dynamics of a single molecule magnet on superconducting Pb(111), Nat. Mater. **19,** 546 (2020).

[64] G. Gabarró-Riera, G. Aromí, and E. C. Sañudo, Magnetic molecules on surfaces: SMMS and beyond, Coord. Chem. Rev. **475,** 214858 (2023).

[65] L. Tesi, F. Stemmler, M. Winkler, S. S. Y. Liu, S. Das, X. Sun, M. Zharnikov, S. Ludwigs, and J. van Slageren, Modular approach to creating functionalized surface arrays of molecular qubits, Adv. Mater. **n/a,** 2208998 (2023).

[66] D. Deutsch and R. Jozsa, Rapid solution of problems by quantum computation, Proc. R. Soc. Lond. A **439,** 553 (1992).

[67] U. L. Heras, A. Mezzacapo, L. Lamata, S. Filipp, A. Wallraff, and E. Solano, Digital Quantum Simulation of Spin Systems in Superconducting Circuits, Phys. Rev. Lett. **112,** 200501 (2014).

[68] J. Ferrando-Soria, S. A. Magee, A. Chiesa, S. Carretta, P. Santini, I. J. Vitorica-Yrezabal, F. Tuna, G. F. Whitehead, S. Sproules, K. M. Lancaster, Anne-Laure Barra, Grigore A. Timco, Eric J. L. McInnes, and Richard E. P. Winpenny, Switchable interactions in molecular double qubits, Chem. **1,** 727 (2016).

[69] S. M. Lewis, M. S. Hunt, G. A. DeRose, H. R. Alty, J. Li, A. Wertheim, L. De Rose, G. A. Timco, A. Scherer, S. G.

Yeates, and R. E. P. Winpenny, Plasma-etched pattern transfer of sub-10 nm structures using a metal–organic resist and helium ion beam lithography, Nano Lett. **19**, 6043 (2019), pMID: 31424217.

[70] M. Fukami, D. R. Candido, D. D. Awschalom, and M. E. Flatté, Opportunities for Long-Range Magnon-Mediated Entanglement of Spin Qubits via On- and Off-Resonant Coupling, PRX Quantum **2**, 040314 (2021).

[71] H. Yuan, Y. Cao, A. Kamra, R. A. Duine, and P. Yan, Quantum magnonics: When magnon spintronics meets quantum information science, Phys. Rep. **965**, 1 (2022).

[72] R. E. George, J. P. Edwards, and A. Ardavan, Coherent Spin Control by Electrical Manipulation of the Magnetic Anisotropy, Phys. Rev. Lett. **110**, 027601 (2013).

[73] J. Liu, J. Mrozek, W. K. Myers, G. A. Timco, R. E. P. Winpenny, B. Kintzel, W. Plass, and A. Ardavan, Electric Field Control of Spins in Molecular Magnets, Phys. Rev. Lett. **122**, 037202 (2019).

[74] J. Liu, J. Mrozek, A. Ullah, Y. Duan, J. J. Baldoví, E. Coronado, A. Gaita-Ariño, and A. Ardavan, Quantum coherent spin–electric control in a molecular nanomagnet at clock transitions, Nat. Phys. **17**, 1205 (2021).

[75] J.-P. Cleuziou, W. Wernsdorfer, V. Bouchiat, T. Ondarcuhu, and M. Monthioux, Carbon nanotube superconducting quantum interference device, Nat. Nanotechnol **1**, 53 (2006).

[76] M. Urdampilleta, S. Klyatskaya, J.-P. Cleuziou, M. Ruben, and W. Wernsdorfer, Supramolecular spin valves, Nat. Mater. **10**, 502 (2011).

[77] C. Godfrin, A. Ferhat, R. Ballou, S. Klyatskaya, M. Ruben, W. Wernsdorfer, and F. Balestro, Operating Quantum States in Single Magnetic Molecules: Implementation of Grover's Quantum Algorithm, Phys. Rev. Lett. **119**, 187702 (2017).